PHYSICAL REVIEW C VOLUME 59, NUMBER 4 APRIL 1999

Semiclassical distorted wave model analysis of multistep direct $(p,p'x)$ and (p,nx) reactions to the continuum

Y. Watanabe,* R. Kuwata, Sun Weili, M. Higashi, and H. Shinohara
Department of Energy Conversion Engineering, Kyushu University, Kasuga, Fukuoka 816-8580, Japan

M. Kohno
Physics Division, Kyushu Dental College, Kitakyushu 803-8580, Japan

K. Ogata and M. Kawai
Department of Physics, Kyushu University, Fukuoka 812-8581, Japan

(Received 3 November 1998)

The semiclassical distorted wave (SCDW) model is extended to include three-step process in multistep direct (MSD) processes in nucleon-induced preequilibrium nucleon-emission reactions. The extended SCDW model is applied to analyses of MSD processes in ^{58}Ni$(p,p'x)$,^{90}Zr$(p,p'x)$,^{90}Zr(p,nx), and ^{209}Bi$(p,p'x)$ in the incident energy range of 62–160 MeV. SCDW calculations with no adjustable parameter give overall good agreement with experimental double differential cross sections, except at very small and large angles. The nonlocality of distorting potentials is taken into account in terms of the Perey factor, and is found to be essential for reproducing the absolute magnitude of the cross sections. Effects of the density and momentum distributions of target nucleons and the use of in-medium N-N cross sections on the SCDW calculation are discussed. Comparison with other models is made, in particular regarding the contributions of individual multistep processes to the calculated cross sections. Validity of the local semiclassical approximation to distorted waves, which is essential to SCDW is discussed on the basis of a numerical test.
[S0556-2813(99)00904-8]

PACS number(s): 24.60.Gv, 24.10.Eq, 25.40.Ep, 25.40.Kv

I. INTRODUCTION

Studies of multistep direct (MSD) processes are important for understanding preequilibrium processes in nucleon-induced reactions at intermediate energies. Various models have been proposed and applied to analyses of experimental data [1]: the intranuclear cascade (INC) model [2], several versions of the exciton model [1], statistical quantum-mechanical (SQM) models of Feshbach, Kerman, and Koonin (FKK) [3], Tamura, Udagawa, and Lenske (TUL) [4], and Nishioka, Weidenmüller, and Yoshida (NWY) [5], and, more recently, microscopic simulation methods based on quantum molecular dynamics (QMD) [6] and antisymmetrized molecular dynamics (AMD) [7].

The SQM models mentioned above are all based on distorted wave Born approximation (DWBA) series expansion of the T-matrix element, with different statistical assumptions in obtaining energy-averaged cross sections [8]. They all contain some adjustable parameters, such as the strength V_0 of effective nucleon-nucleon interactions, for fitting the calculated results with experimental data. The semiclassical distorted wave (SCDW) model [9–11] that we discuss in the present paper is based on the DWBA series expansion of the T-matrix element, the local semiclassical approximation to distorted waves, the eikonal approximation to intermediate state Green functions, and the local density Fermi gas model for the nuclear states. The double differential cross sections of one-, two-, and three-step processes are expressed in the simple closed forms of Eqs. (13), (16), and (17) in Sec. II, respectively, in terms of the distorted waves, the nucleon-nucleon scattering cross sections, and the nucleon density distribution. Since those quantities can be determined either empirically or theoretically, no free adjustable parameter is involved in the SCDW model. Furthermore, the expressions for the cross sections allow a simple intuitive interpretation that the reaction proceeds via successive nucleon-nucleon collisions at different points in the nucleus, which is one of the basic assumptions of the INC model. In this sense, the SCDW model has a possibility of bridging the SQM models and the microscopic simulation methods of INC, QMD, and AMD.

Calculations of the one-step $(p,p'x)$ cross sections with the SCDW model were previously carried out in the incident energy range of 62–200 MeV [9,11]. The calculated double differential inclusive $(p,p'x)$ cross sections agreed with experimental data at forward, though not extremely forward, angles and relatively high emission energies. Agreement in the absolute magnitude was significant because of no free parameter in the model. However, the calculated one-step cross sections were much smaller than the experimental data at large angles and/or low emission energies that correspond to large momentum transfers. This clearly indicates the importance of multistep processes in such cases. Extension of the SCDW model to two-step processes was made in Ref. [10] in which an explicit formula for the double differential cross section of two-step processes was derived.

In the present work, we extend the analysis including up to three-step processes, and present the results of numerical

---

*Present address: Department of Advanced Energy Engineering Science, Kyushu University, Fukuoka, Japan.

calculations for $(p,p'x)$ and (p,nx) at energies ranging from 62 MeV to 160 MeV. The results are compared with experimental data and with calculations by other models. We show the contribution of individual multistep processes to the cross section and the effect of the nonlocality of distorting potentials, the density and momentum distributions of target nucleons, and the use of in-medium *N*-*N* scattering cross sections on the SCDW cross sections. We also discuss the validity of the local semiclassical approximation to distorting potentials that is the most essential approximation in the SCDW model.

The formulation of the SCDW model including three-step processes is briefly described in Sec. II. The results of the calculations are presented and compared with experimental data in Secs. III A and III B. Discussions are given on the validity of the local semiclassical approximation to distorted waves, the effects of the nonlocality corrections, the quasielastic scattering, the nucleon density and momentum distributions, and the use of in-medium *N*-*N* cross sections on SCDW calculations in Secs. III C–III H. Comparisons with other models are discussed in Sec. III I. A summary and conclusions are given in Sec. IV.

II. FORMULATION

As the past SQM models already mentioned, the SCDW model is based on DWBA series expansion of the *T*-matrix element

$$T_{n0}=\langle\chi_f^{(-)}\Phi_n|V+VGV+VGVGV+\cdots|\Phi_0\chi_i^{(+)}\rangle, \quad (1)$$

where Φ_0 (Φ_n) is the nuclear wave function in the ground (the nth excited final) state, $\chi_i^{(+)}$ ($\chi_f^{(-)}$) is the distorted wave in the initial (final) channel, *V* is the interaction potential between the leading particle 0 and the nucleus *A*, and the *G*'s are the Green functions for the motion of 0 relative to *A* in the intermediate states. We assume the single particle model for the nuclear states, and the sum of the two-nucleon interaction potentials between 0 and individual target nucleons, *i*, for *V*:

$$V=\sum_{i=1}^{A} v(\mathbf{r}_0-\mathbf{r}_i), \quad (2)$$

where $\mathbf{r}_0$ and $\mathbf{r}_i$ are the coordinates of the incident and target nucleons, respectively. *V* is assumed to be spin and isospin independent, for the moment, for the sake of simplicity of explanation. The dependence is included in the actual calculations reported in the subsequent sections. In addition, we introduce the "never come back" assumption [12] that the number of excited particle-hole pairs increases with the number of steps of the reaction process. Using these assumptions, we arrive at the expression for the inclusive double differential cross section of emission of a nucleon at energy E_f and into direction Ω_f at incident energy E_i:

$$\frac{\partial^2\sigma}{\partial E_f\partial\Omega_f}=\sum_N \frac{\partial^2\sigma^{(N)}}{\partial E_f\partial\Omega_f}, \quad (3)$$

where

$$\frac{\partial^2\sigma^{(N)}}{\partial E_f\partial\Omega_f}=\frac{\mu^2}{(2\pi\hbar^2)^2}\frac{k_f}{k_i} \times\sum_n |\langle\chi_f^{(-)}\Phi_n|V(GV)^{N-1}|\Phi_0\chi_i^{(+)}\rangle|^2 \times\delta(\varepsilon_n-\varepsilon_0-\omega) \quad (4)$$

is the cross section of *N*-step process. Since the different *N*'s correspond to different final states, the cross terms between them do not exist in Eq. (3). In Eq. (4), μ is the reduced mass, k_i (k_f) is the incident (outgoing) wave number, ε_0 (ε_n) is the nuclear energy in the initial (final) state, and $\omega=E_i-E_f+Q$ where *Q* is zero for $(p,p'x)$ and *Q* is the ground state *Q* value for (p,nx). The summation is made over all the final *n* states. The δ function ensures energy conservation.

In each step of the MSD process, a target nucleon collides with the leading particle 0 and is excited from a single particle state ϕ_α at ε_α below the Fermi level, *F*, to a state ϕ_β at ε_β above *F*. For a one-step cross section, then, the right-hand side (RHS) of Eq. (4) becomes a sum over α and β of the squared modulus of the transition matrix element for the transition $\alpha\rightarrow\beta$ which is a twofold integral over the coordinate of the leading particles, $\mathbf{r}_0$, and that of the struck nucleon, $\mathbf{r}$. On expanding the squared modulus, one has a four-fold integral over $\mathbf{r}_0,\mathbf{r}_0',\mathbf{r}$, and $\mathbf{r}'$ as below:

$$\frac{\partial^2\sigma^{(1)}}{\partial E_f\partial\Omega_f}=\frac{4\mu^2}{(2\pi\hbar^2)^2}\frac{k_f}{k_i}\int d\mathbf{r}d\mathbf{r}'d\mathbf{r}_0d\mathbf{r}_0'\chi_f^{(-)*}(\mathbf{r}_0) \times v(\mathbf{r}_0,\mathbf{r})\chi_i^{(+)}(\mathbf{r}_0) \times\chi_f^{(-)}(\mathbf{r}_0')v(\mathbf{r}_0',\mathbf{r}')\chi_i^{(+)*}(\mathbf{r}_0')K(\mathbf{r},\mathbf{r}'), \quad (5)$$

where the nonlocal kernel $K(\mathbf{r},\mathbf{r}')$ is given by

$$K(\mathbf{r},\mathbf{r}')=\sum_{\beta>F}\sum_{\alpha<F}\phi_\beta(\mathbf{r})^*\phi_\alpha(\mathbf{r})\phi_\beta(\mathbf{r}') \times\phi_\alpha^*(\mathbf{r}')\delta(\varepsilon_\beta-\varepsilon_\alpha-\omega). \quad (6)$$

Because of the closure property of the ϕ, it is easy to see that $K(\mathbf{r},\mathbf{r}')$ is only appreciable when $\mathbf{r}\approx\mathbf{r}'$ unless the number of ε_α states is too small. Because of this and the short range of the potential *V*, the integrand of the four-fold integral in Eq. (5) is only appreciable when $\mathbf{r}\approx\mathbf{r}'\approx\mathbf{r}_0\approx\mathbf{r}_0'$.

Under these circumstances, the following two approximations are introduced in the SCDW model. The first one is the local semi-classical approximation (LSCA) for the distorted waves, $\chi_c(\mathbf{r}_0)$, in the distorting potentials $U_c(\mathbf{r}_0)$ of which the spin-orbit coupling is neglected:

$$\chi_c(\mathbf{r}_0')\approx\chi_c(\mathbf{r}_0)e^{i\mathbf{k}_c(\mathbf{r}_0)\cdot(\mathbf{r}_0'-\mathbf{r}_0)} \quad (c=i,f), \quad (7)$$

for $\mathbf{r}_0'$ within a small cell centered at $\mathbf{r}_0$ in which U_c changes little. In Eq. (7), $\mathbf{k}_c(\mathbf{r}_0)=-i\nabla\chi_c(\mathbf{r}_0)/\chi_c(\mathbf{r}_0)$ is the local wave number vector with $k_c(\mathbf{r}_0)=\{2\mu/\hbar^2[E_c-U_c(\mathbf{r}_0)]\}^{1/2}$, which is approximately real and proportional to the flux if the imaginary part of U_c is small compared with the local kinetic energy at the point $\mathbf{r}_0$. We neglect the imaginary part of $k_c(\mathbf{r}_0)$: $k_c(\mathbf{r}_0)\approx\mathrm{Re}[k_c(\mathbf{r}_0)]$. The validity of the LSCA in the SCDW model will be discussed in Sec. III C.

The second assumption which greatly facilitates the subsequent calculations is the local density Fermi gas (LFG) model for the nuclear states. Within a small cell centered at $\mathbf{r}\approx\mathbf{r}'$, the ϕ are approximated by plane waves with the Fermi level at the Fermi momentum k_F, which is related to the nucleon density $\rho(\mathbf{r})$ at $\mathbf{r}$:

$$\rho(\mathbf{r})=4\frac{4\pi}{3}\frac{k_F^3(\mathbf{r})}{(2\pi)^3}. \tag{8}$$

As a result, $K(\mathbf{r},\mathbf{r}')$ given by Eq. (6) is a function of $x\equiv|\mathbf{r}-\mathbf{r}'|$, i.e., $K=K(x)$. Explicit calculation [9] shows that the range of $K(x)$ is indeed short, much shorter than the diameter of the medium-heavy nuclei of our present interest.

Using the two approximations, the one-step cross section becomes

$$\begin{aligned}\frac{\partial^2\sigma^{(1)}}{\partial E_f\partial\Omega_f}=&\frac{4\mu^2}{(2\pi\hbar^2)^2}\frac{k_f}{k_i}\frac{1}{(2\pi)^3}\int d\mathbf{r}_0|\chi_f^{(-)}(\mathbf{r}_0)|^2|\chi_i^{(+)}(\mathbf{r}_0)|^2\\&\times\int\int_{k_\alpha<k_F(\mathbf{r}_0)<k_\beta}d\mathbf{k}_\alpha d\mathbf{k}_\beta\left|\int d\boldsymbol{\rho}v(\boldsymbol{\rho})e^{i\mathbf{q}(\mathbf{r}_0)\cdot\boldsymbol{\rho}}\right|^2\\&\times\delta(\mathbf{k}_\beta-\mathbf{k}_\alpha+\mathbf{k}_f(\mathbf{r}_0)-\mathbf{k}_i(\mathbf{r}_0))\delta(\varepsilon_\beta-\varepsilon_\alpha-\omega),\end{aligned} \tag{9}$$

where $\boldsymbol{\rho}=\mathbf{r}-\mathbf{r}_0$, and $\mathbf{q}(\mathbf{r}_0)$ is the local momentum transfer, $\mathbf{k}_i(\mathbf{r}_0)-\mathbf{k}_f(\mathbf{r}_0)$. The first δ function in Eq. (9) ensures momentum conservation and the second one energy conservation. In the previous SCDW calculations of $(p,p'x)$ [9–11], the energy delta function was approximated by replacing ω by the difference in the local kinetic energies of the incident and the outgoing nucleons. Thus, in the LFG model,

$$\varepsilon_\beta-\varepsilon_\alpha-\omega\approx\frac{\hbar^2}{2\mu}[k_\beta^2-k_\alpha^2-k_i(\mathbf{r}_0)^2+k_f(\mathbf{r}_0)^2]. \tag{10}$$

This approximation is only good if the distorting potentials in the initial and the final channels, U_i and U_f, respectively, are nearly equal, $U_i\approx U_f$, and the ground state Q value is zero as in $(p,p'x)$ or negligibly small. The delta function implies conservation of the total kinetic energy of the colliding two nucleons, i.e., ''on-the-energy-shell'' N-N scattering. In general, however, the approximation $U_i\approx U_f$ may not be as good, and the Q value may not be negligible in (p,nx) reactions. Then, ω should be taken exactly and Eq. (10) should be replaced by

$$\varepsilon_\beta-\varepsilon_\alpha-\omega=\frac{\hbar^2}{2\mu}(k_\beta^2-k_\alpha^2)-\{(E_i-E_f)+(S_\beta-S_\alpha)\}, \tag{11}$$

since $Q=S_\beta-S_\alpha$ where $S_\gamma(\gamma=\alpha,\beta)$ is the separation energy of the struck target nucleon. The conservation of the total kinetic energy of the two-nucleon system, therefore, does not hold. Strictly speaking, off-the-energy-shell matrix elements of N-N scattering are needed. We assume, however, that the squared modulus of the matrix element of v is still proportional to the free N-N scattering cross section for the two-body c.m. energy corresponding to the initial relative momentum $\boldsymbol{\kappa}=(\mathbf{k}_i(\mathbf{r}_0)-\mathbf{k}_\alpha)/2$ and the scattering angle equal to the angle between $\boldsymbol{\kappa}$ and the final relative momentum, $\boldsymbol{\kappa}'=[\mathbf{k}_f(\mathbf{r}_0)-\mathbf{k}_\beta]/2$:

$$\left(\frac{\partial\sigma}{\partial\Omega_{\boldsymbol{\kappa}}}\right)_{NN}=\frac{(m/2)^2}{(2\pi\hbar^2)^2}\left|\int d\boldsymbol{\rho}v(\boldsymbol{\rho})e^{-i\mathbf{q}(\mathbf{r}_0)\cdot\boldsymbol{\rho}}\right|^2, \tag{12}$$

where m is the nucleon mass. Inserting Eq. (12) into Eq. (9) and replacing $\mathbf{r}_0$ by $\mathbf{r}$, one obtains the final expression of one-step double differential cross section:

$$\begin{aligned}\frac{\partial^2\sigma^{(1)}}{\partial E_f\partial\Omega_f}=&\left(\frac{A}{A+1}\right)^2\int d\mathbf{r}\frac{k_f/k_f(\mathbf{r})}{k_i/k_i(\mathbf{r})}|\chi_i^{(+)}(\mathbf{r})|^2\\&\times|\chi_f^{(-)}(\mathbf{r})|^2\left(\frac{\partial^2\sigma}{\partial E_f\partial\Omega_f}\right)_{\mathbf{r}}\rho(\mathbf{r}),\end{aligned} \tag{13}$$

where A is the target mass number, and the local average differential cross section of N-N scattering at the point $\mathbf{r}$ is now given by

$$\begin{aligned}\left(\frac{\partial^2\sigma}{\partial E_f\partial\Omega_f}\right)_{\mathbf{r}}=&\frac{4\mu k_f(\mathbf{r})}{\hbar^2k_i(\mathbf{r})(4\pi/3)k_F(\mathbf{r})^3}\\&\times\int\int_{k_\alpha<k_F(\mathbf{r})<k_\beta}d\mathbf{k}_\alpha d\mathbf{k}_\beta\left(\frac{\partial\sigma}{\partial\Omega_{\boldsymbol{\kappa}}}\right)_{NN}\\&\times\delta(\mathbf{k}_\beta-\mathbf{k}_\alpha+\mathbf{k}_f(\mathbf{r})-\mathbf{k}_i(\mathbf{r}))\delta(\varepsilon_\beta-\varepsilon_\alpha-\omega),\end{aligned} \tag{14}$$

which involves the approximate treatment of the off-shell matrix element of v already mentioned. The Pauli blocking effect is taken into account in Eq. (14) by the limits of the integrations over $\mathbf{k}_\alpha$ and $\mathbf{k}_\beta$. The local kinetic energy $E_f(\mathbf{r})=\hbar^2k_f(\mathbf{r})^2/2\mu$ and the direction of emission, $\Omega_f(\mathbf{r})=\hat{\mathbf{k}}_f(\mathbf{r})$, correspond to E_f and Ω_f at infinity, respectively.

In the calculation of two- and three-step cross sections, the eikonal approximation is made to the intermediate Green function as an additional approximation [10]:

$$\left\langle\mathbf{r}_2\left|\frac{1}{E_m-K-U_m+i\eta}\right|\mathbf{r}_1\right\rangle\approx-\frac{\mu}{2\pi\hbar^2}\frac{\exp(ik_m|\mathbf{r}_2-\mathbf{r}_1|)}{|\mathbf{r}_2-\mathbf{r}_1|}, \tag{15}$$

where $\mathbf{r}_1$ ($\mathbf{r}_2$) is the first (second) collision point, and $k_m=[(2\mu/\hbar^2)(E_m-U_m)]^{1/2}=\kappa_m+i\gamma_m$ is the complex local wave number in the intermediate state.

The final form of the two-step SCDW cross section is given, in agreement with Ref. [10], by

$$\frac{\partial^2\sigma^{(2)}}{\partial E_f\partial\Omega_f}=\left(\frac{A}{A+1}\right)^4\int dE_m\int d\mathbf{r}_1\int d\mathbf{r}_2\,\frac{k_f/k_f(\mathbf{r}_2)}{k_i/k_i(\mathbf{r}_1)}|\chi_f^{(-)}(\mathbf{r}_2)|^2|\chi_i^{(+)}(\mathbf{r}_1)|^2\left(\frac{\partial^2\sigma}{\partial E_f\partial\Omega_f}\right)_{\mathbf{r}_2}\rho(\mathbf{r}_2)$$

$$\times\frac{\exp(-2\gamma_m|\mathbf{r}_2-\mathbf{r}_1|)}{|\mathbf{r}_2-\mathbf{r}_1|^2}\left(\frac{\partial^2\sigma}{\partial E_m\partial\Omega_m}\right)_{\mathbf{r}_1}\rho(\mathbf{r}_1), \tag{16}$$

where $E_m=\hbar^2\kappa_m^2/2\mu$ and Ω_m is the direction of $\mathbf{r}_2-\mathbf{r}_1$. The local average cross sections are given by Eq. (14) with appropriate substitutions of coordinates and momenta. Again, the off-shell matrix elements of the N-N collisions are approximately treated. The extension to higher step processes is straightforward and the following expression for the three-step cross section is obtained:

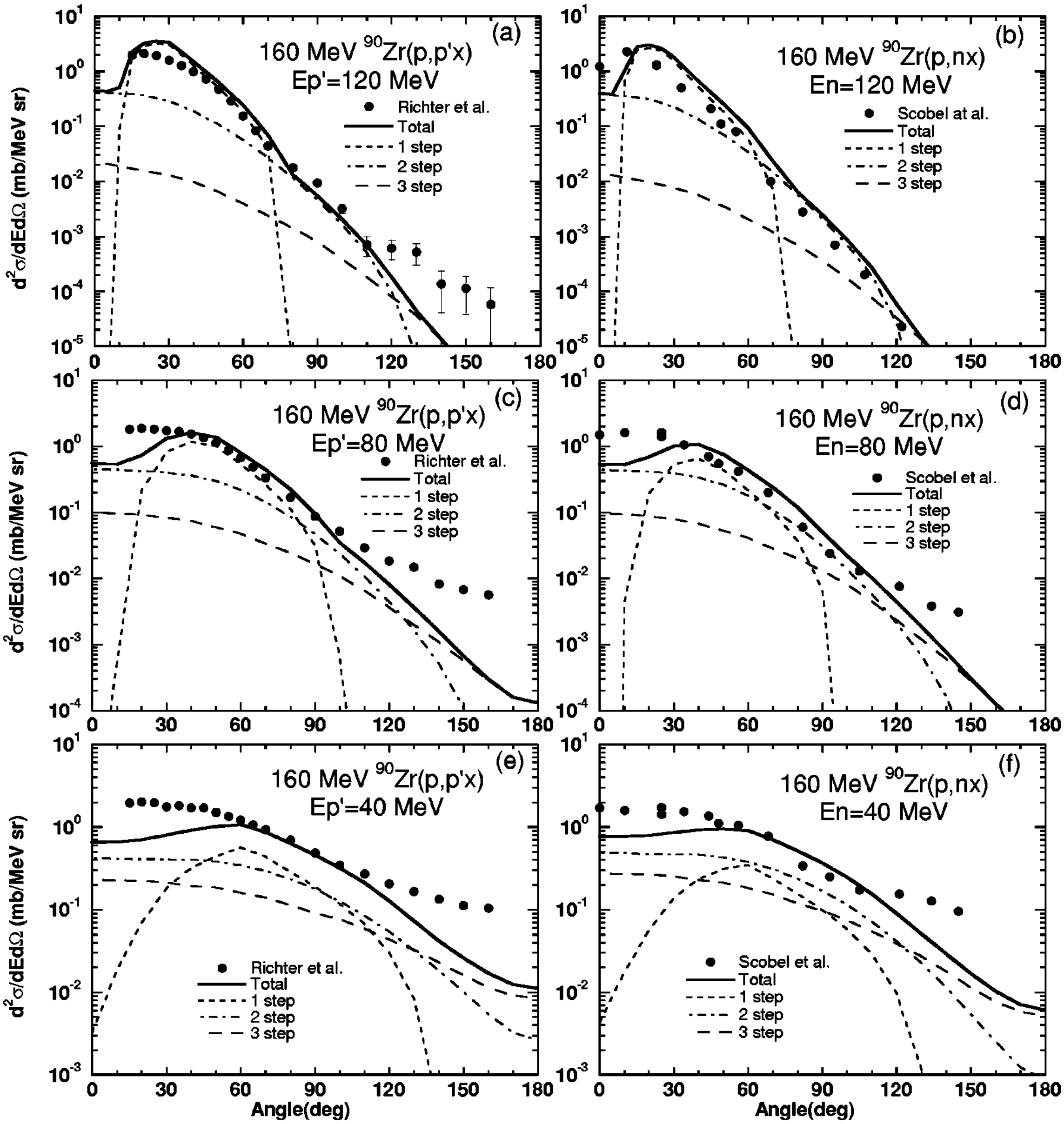

FIG. 1. Comparison between theoretical and measured double differential cross sections for $(p,p'x)$ and (p,nx) on ^{90}Zr at 160 MeV for three emission energies of 120 MeV, 80 MeV, and 40 MeV. The left [right] panel corresponds to $(p,p'x)[(p,nx)]$. The cross sections of one-step, two-step, and three-step processes are represented by the short-dashed, the dash-dotted, and the long-dashed curves, respectively. The solid curves are their sum. The experimental data are taken from Ref. [23] for $(p,p'x)$ and Ref. [26] for (p,nx).

$$\frac{\partial^2\sigma^{(3)}}{\partial E_f\partial\Omega_f}=\left(\frac{A}{A+1}\right)^6\int dE_{m1}\int dE_{m2}\int d\mathbf{r}_1\int d\mathbf{r}_2\int d\mathbf{r}_3\frac{k_f/k_f(\mathbf{r}_3)}{k_i/k_i(\mathbf{r}_1)}|\chi_f^{(-)}(\mathbf{r}_3)|^2|\chi_i^{(+)}(\mathbf{r}_1)|^2$$
$$\times\left(\frac{\partial^2\sigma}{\partial E_f\partial\Omega_f}\right)_{\mathbf{r}_3}\rho(\mathbf{r}_3)\frac{\exp[-2\gamma_{m2}|\mathbf{r}_3-\mathbf{r}_2|]}{|\mathbf{r}_3-\mathbf{r}_2|^2}\left(\frac{\partial^2\sigma}{\partial E_{m2}\partial\Omega_{m2}}\right)_{\mathbf{r}_2}\rho(\mathbf{r}_2)\frac{\exp[-2\gamma_{m1}|\mathbf{r}_2-\mathbf{r}_1|]}{|\mathbf{r}_2-\mathbf{r}_1|^2}\left(\frac{\partial^2\sigma}{\partial E_{m1}\partial\Omega_{m1}}\right)_{\mathbf{r}_1}\rho(\mathbf{r}_1). \tag{17}$$

In the case of $(p,p'x)$ reactions, there are two types of two-step processes, $(p,p'')(p'',p')$ and $(p,n)(n,p')$, with either a proton or a neutron in the intermediate state. Similarly, a three-step process consists of four different reaction paths: $(p,p'')(p'',p''')(p''',p')$, $(p,p'')(p'',n)(n,p')$, $(p,n)(n,p'')(p'',p')$, and $(p,n)(n,n')(n',p')$.

The empirical local optical potentials that we use for the distorting potentials should be regarded as the equivalent local potentials of the "true" nonlocal optical potentials. As is well known, the amplitude of a distorted wave in the nonlocal optical potential is less than that in the local optical potential by the Perey factor with the nonlocality range β [13],

$$F_c(\mathbf{r})=\left(1-\frac{\mu\beta^2U_c(\mathbf{r})}{2\hbar^2}\right)^{-1/2}, \tag{18}$$

multiplying the wave functions of all the particles in the continuum, namely, the leading particles in the initial and final channels and the struck target nucleon in state ε_β in the continuum. The Perey factor is unity for bound state wave functions in the Fermi gas model because of the normalization. In addition, we multiply the Green function by $F_m(\mathbf{r}_1)$ and $F_m(\mathbf{r}_2)$ on either side of it in Eq. (15).

III. RESULTS AND DISCUSSIONS

A. Input data for numerical calculations

As seen in Eqs. (13), (16), and (17), the input data for SCDW calculations are (a) the distorting potentials, (b) the two-nucleon scattering cross sections, and (c) the nucleon density distribution. We use basically the same input data as in Ref. [11].

As for (a), we adopted the global optical potentials of Walter and Guss [14] for energies less than 80 MeV and those of Schwandt *et al.* [15] for energies above 80 MeV. For neutrons, however, the real part of the optical potential parameters of Ref. [15] was modified by means of Madland's method [16]. The range of nonlocality, β, in Eq. (18) was taken to be 0.85 fm [13].

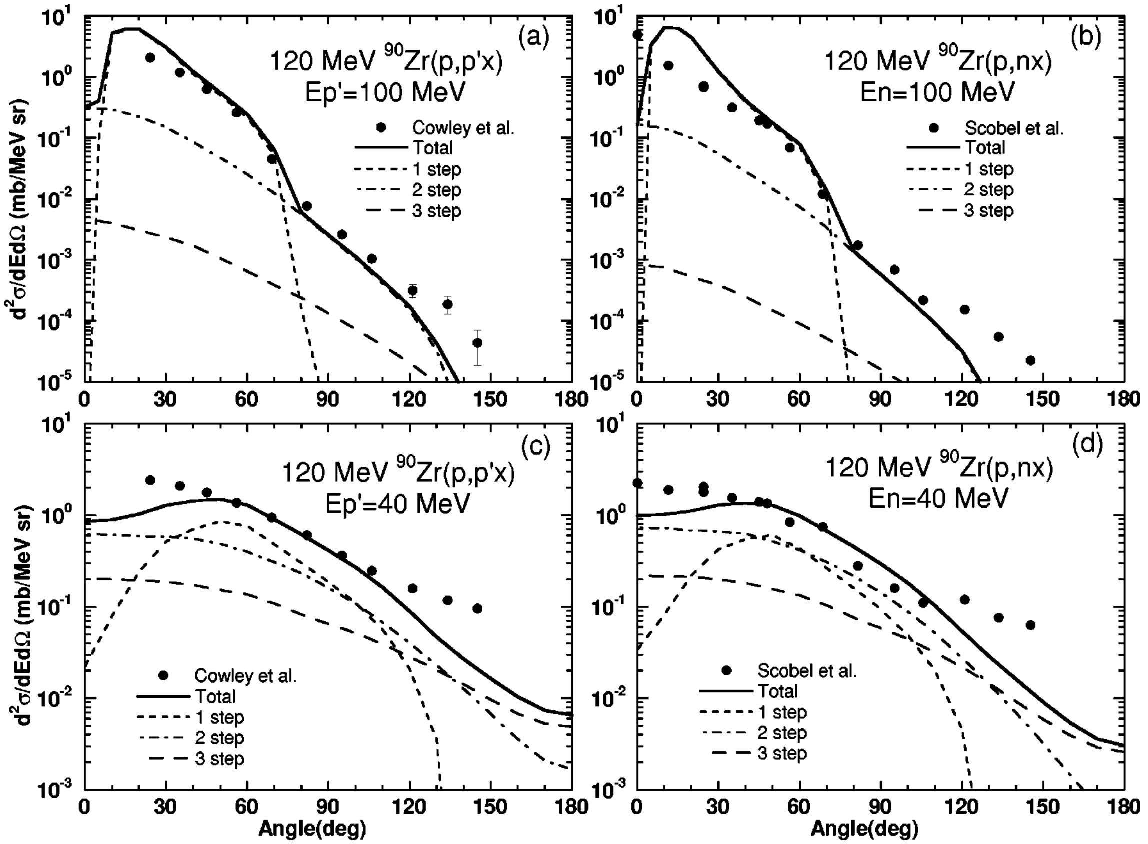

FIG. 2. The same as in Fig. 1, but for $(p,p'x)$ and (p,nx) on ^{90}Zr at 120 MeV for two emission energies of 100 MeV and 40 MeV. The experimental data are taken from Ref. [24] for $(p,p'x)$ and Ref. [26] for (p,nx).

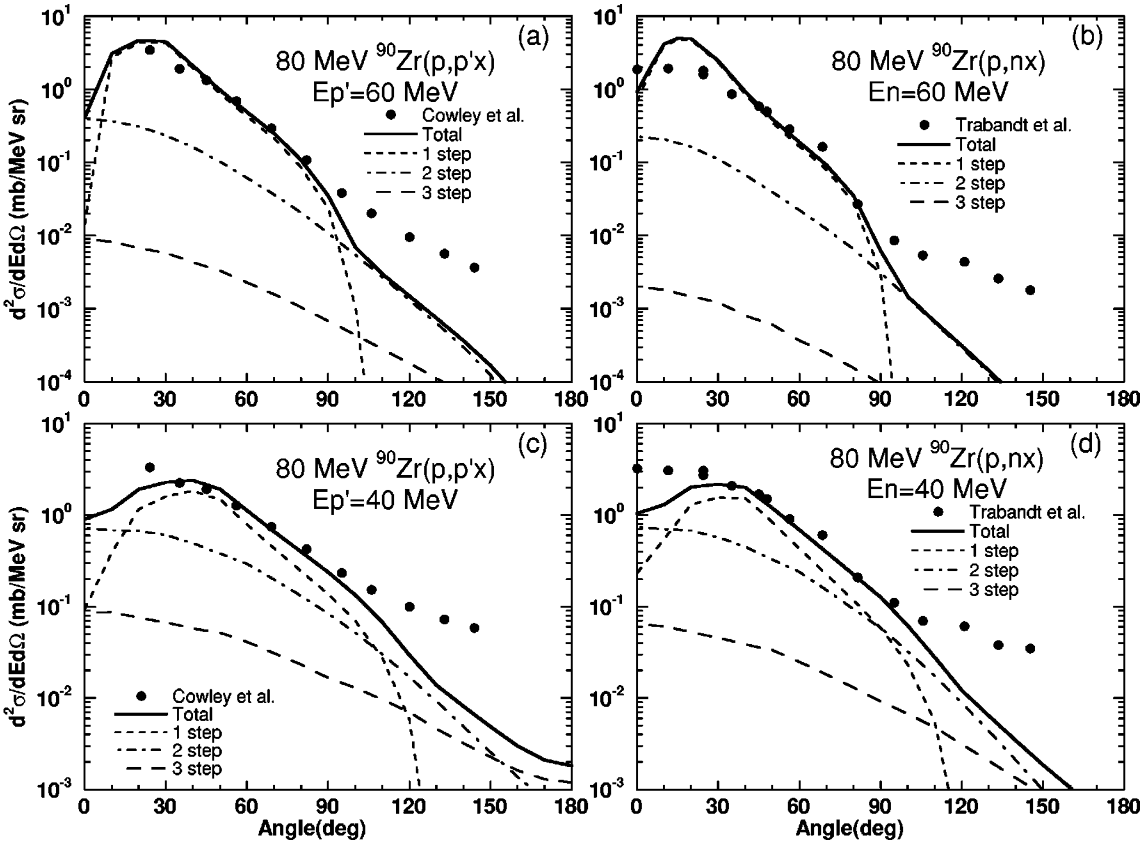

FIG. 3. The same as in Fig. 1, but for $(p,p'x)$ and (p,nx) on ^{90}Zr at 80 MeV for two emission energies of 60 MeV and 40 MeV. The experimental data are taken from Ref. [24] for $(p,p'x)$ and Ref. [25] for (p,nx).

As for (b), either two-nucleon scattering cross sections in free space or those in nuclear medium were used. For the free *N*-*N* cross sections, we used the same empirical formula as in Ref. [11], i.e., the parametrized total and differential cross sections taken from Ref. [18] and Ref. [19], respectively. For the in-medium *N*-*N* cross sections, we employed the nonrelativistic Brueckner *G*-matrix calculated with the Paris potential given by Kohno *et al.* [20]. In both cases, the parameters were given as a function of the energy of the *N*-*N* system in the laboratory frame. We took for it the kinetic energy of relative motion in the initial channel.

As for (c), we used the nucleon density distribution $\rho(r)$ of the Woods-Saxon shape with Negele's geometrical parameters [17], and assumed that the proton and the neutron densities are proportional to their numbers Z and N, $\rho(r)_p = (Z/A)\rho(r)$ and $\rho(r)_n = (N/A)\rho(r)$, respectively. The local Fermi momentum $k_F(\mathbf{r})$ necessary for the calculation of Eq. (14) was obtained from Eq. (8), for both protons and neutrons.

B. Comparison with the experimental angular distributions

Using a Monte Carlo integration method with quasirandom numbers [21,22], we have carried out SCDW calculations including up to three-step processes of the double differential cross sections of ^{90}Zr$(p,p'x)$ and (p,nx) reactions at 80, 120, and 160 MeV, ^{58}Ni$(p,p'x)$ at 120 MeV, and ^{209}Bi$(p,p'x)$ at 62 MeV. The free *N*-*N* scattering cross sections have been used in the calculations.

Figures 1–3 show the calculated and experimental double differential cross sections of $(p,p'x)$ and (p,nx) on ^{90}Zr [23–26]. The contributions of individual multistep processes are plotted to show their variation with emission energy and scattering angle; the short-dashed, the dash-dotted, and the long-dashed lines represent cross sections of one-, two-, and three-step processes, respectively. The solid lines represent their sum. The SCDW calculations, with no free adjustable parameter, are in overall good agreement with the experimental data except at very small and large angles, for both $(p,p'x)$ and (p,nx). For the highest emission energy shown in the figures, however, the SCDW cross section has a peak around 20° and is larger than the experimental data by a factor of about 2. Similar peaks in the angular distributions are also seen at other emission energies, although the peaks become broader as proton emission energy decreases.

One can see that proton emission via one-step process is dominant in the intermediate angular region. Contributions of two- and three-step processes become appreciable with decreasing emission energies and increasing angles. It is found, however, that the higher-step MSD components cannot compensate the discrepancy between the one-step cross sections and the experimental data at backward angles. As will be discussed later, one of the reasons for this is probably that in the LFG model that we assumed, the nucleons can only have momenta up to the Fermi momentum. Another possibility might be that MSD contributions from higher steps are not included in the present calculation. At very forward angles, the one-step cross sections fall off steeply toward 0° at all outgoing energies, as was already seen in

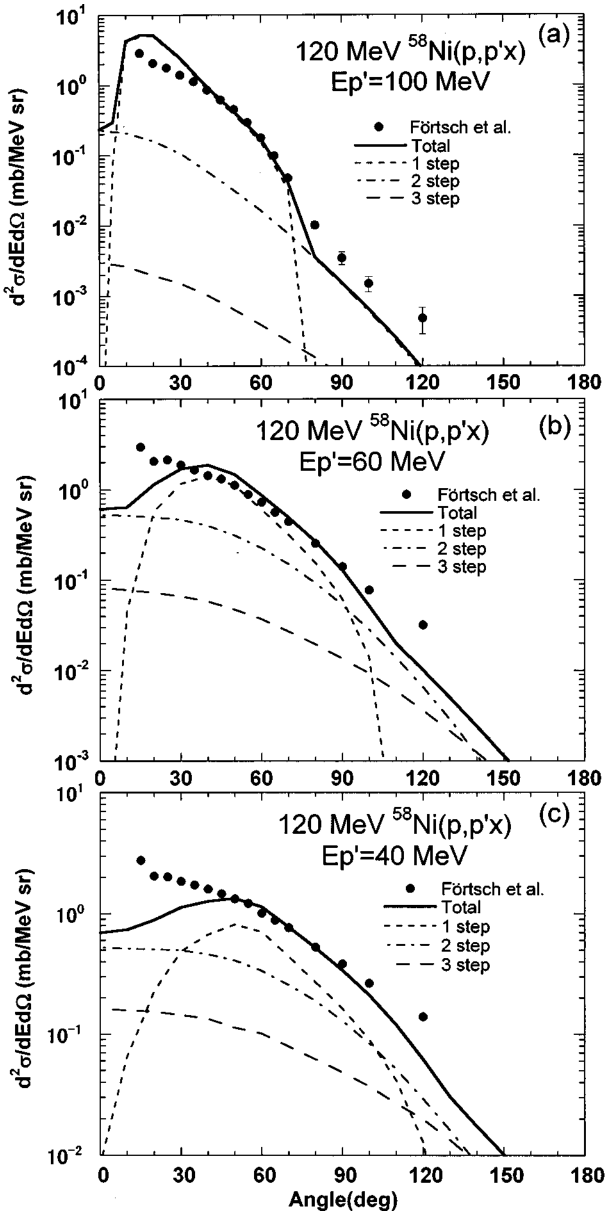

FIG. 4. Comparison between theoretical and measured double differential cross sections for the reaction ^{58}Ni$(p,p'x)$ at 120 MeV for three emission energies of (a) 100 MeV, (b) 60 MeV, and (c) 40 MeV. The cross sections of one-step, two-step, and three-step processes are represented by the short-dashed, the dash-dotted, and the long-dashed curves, respectively. The solid curves are their sum. The experimental data are taken from Ref. [27].

our previous calculation [11]. In contrast, the two-step and three-step cross sections have maxima at 0°. The broad peak structures seen in the summed cross sections are due to the characteristic shape of one-step angular distributions. The peak angles are nearly at the quasielastic scattering (QES) peaks. The influence of QES on the one-step process will be discussed in a later subsection.

Figure 4 shows the calculated angular distributions of ^{58}Ni$(p,p'x)$ at 120 MeV compared with the experimental data [27]. Agreement is very similar to the case of ^{90}Zr; there are some discrepancies at small and large angles and underestimation at the lowest emission energy.

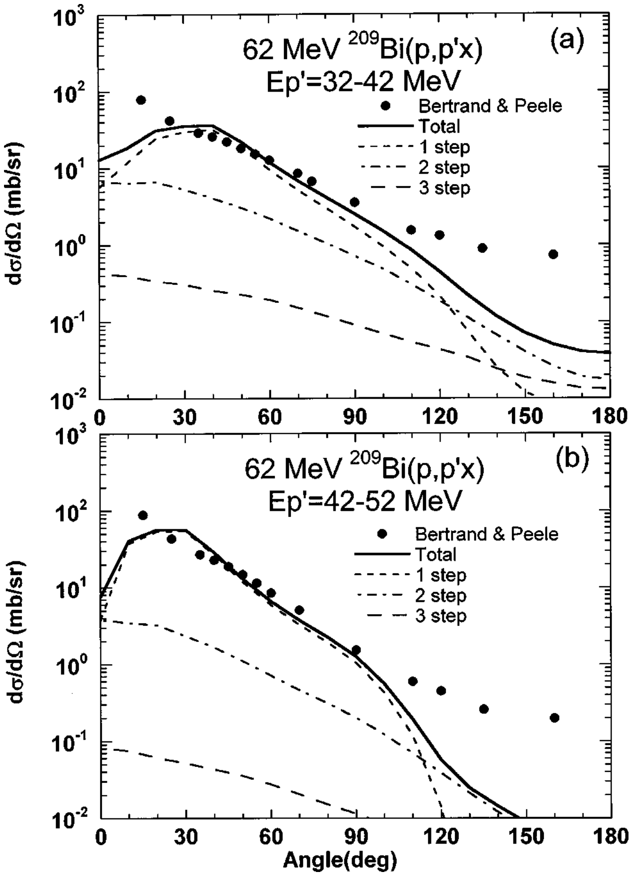

FIG. 5. Comparison between theoretical and measured angular distributions for the reaction ^{209}Bi$(p,p'x)$ at 62 MeV for two emission energy range of (a) 32–42 MeV and (b) 42–52 MeV. The cross sections of one-step, two-step, and three-step processes are represented by the short-dashed, the dash-dotted, and the long-dashed curves, respectively. The solid curves are their sum. The experimental data are taken from Ref. [28].

Figures 3 and 5 show the SCDW results for $(p,p'x)$ and (p,nx) on ^{90}Zr at 80 MeV and $(p,p'x)$ on ^{209}Bi at 62 MeV, respectively, to indicate the applicability of the SCDW model to lower incident energies. The SCDW model reproduces well the experimental data at forward, though not very forward, angles where the one-step process is dominant. The cross sections of the higher-order steps are only small fractions of the total, even at backward angles, and the summed cross sections are much smaller than the experimental ones at large angles. Another feature is that the one-step cross sections do not fall so steeply toward 0° as in the cases of higher incident energies. This is due to the deeper real part of the distorting potentials which causes stronger refraction of the entrance and the exit channel distorted waves than at the higher incident energies. In fact, if one neglects the distorting potentials, the one-step angular distributions drop more steeply toward 0° and reach zero at an angle near 0°.

C. Validity of the local semiclassical approximation to distorted waves

For the SCDW model, it is important to verify the LSCA to distorted waves, Eq. (7). We have carried out a numerical test of the LSCA for two incident energies, 26 and 120 MeV, for the case of the $n+{}^{58}$Ni reaction. We compared an ‘‘ex-

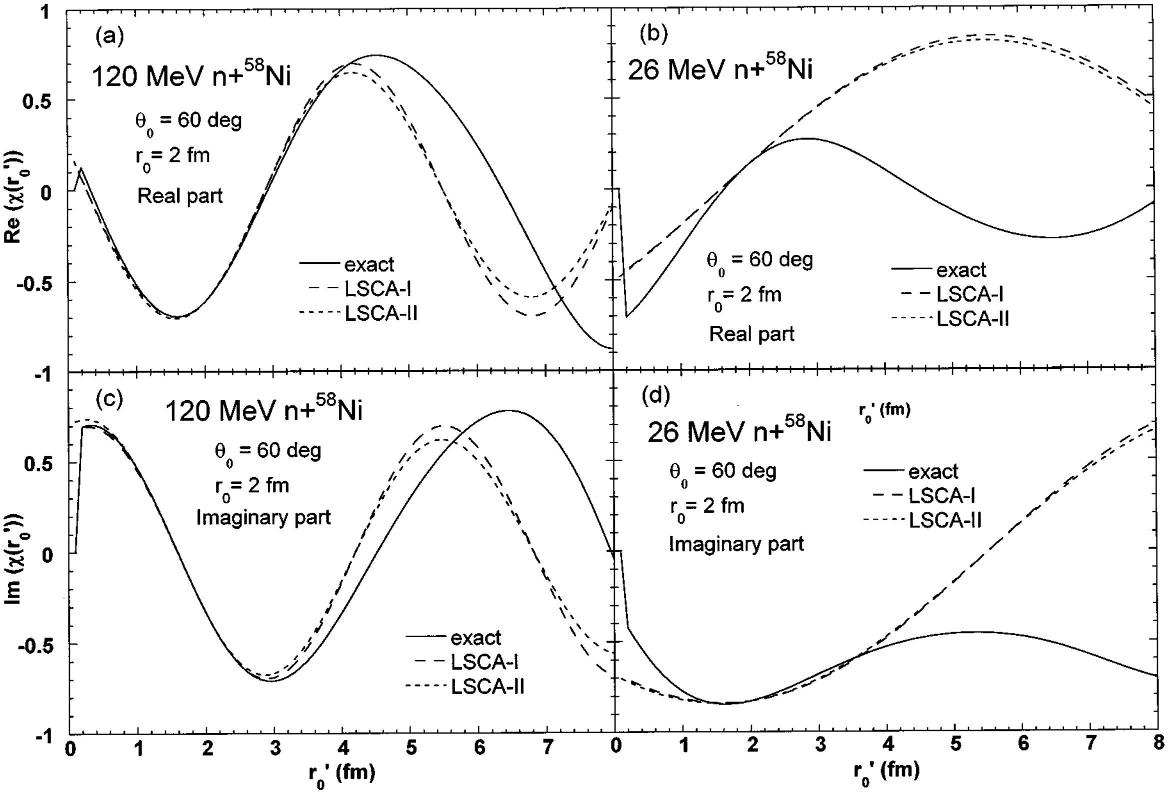

FIG. 6. Comparisons of ‘‘exact’’ and ‘‘LSCA’’ distorted waves of a neutron in ^{58}Ni. The left (right) panel is the result for incident energies 120 MeV (26 MeV). The real (imaginary) part is shown in the upper (lower) panel. LSCA-I (LSCA-II) represents LSCA with the real (complex) wave number. The distorted waves are plotted as a function of r_0' at $r_0=2$ fm and $\theta_0=60°$.

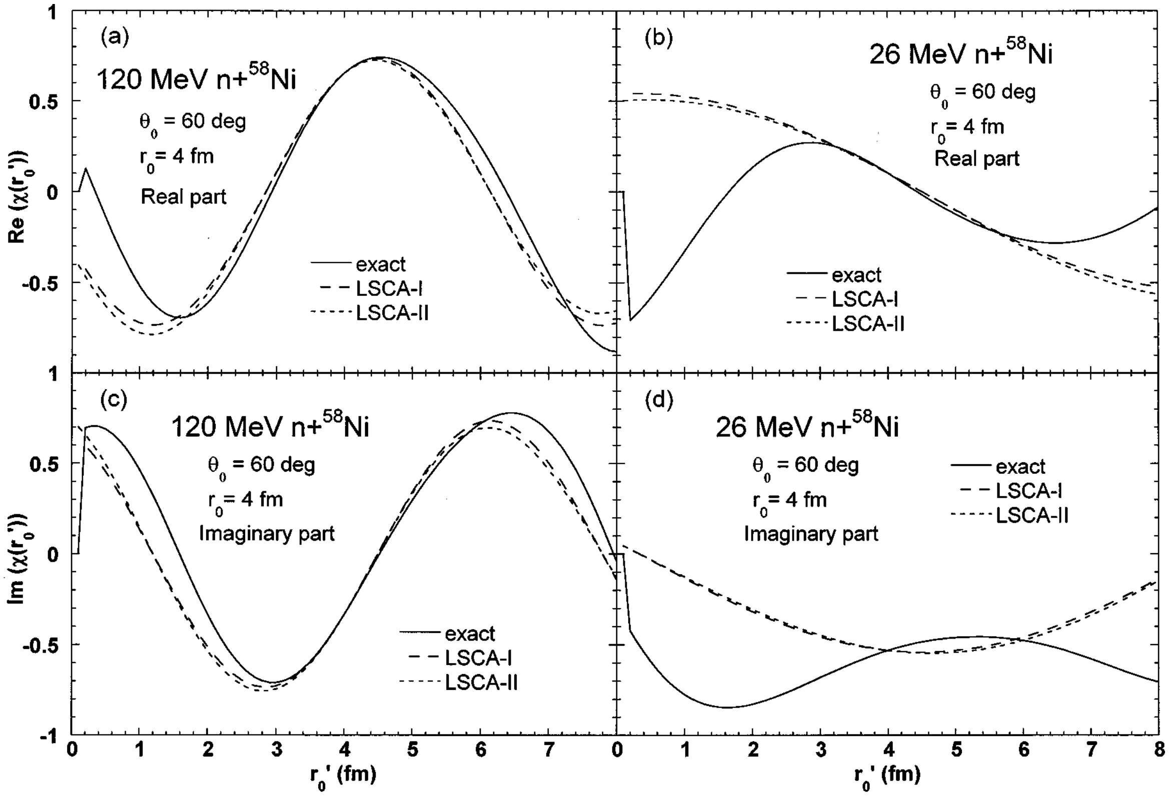

FIG. 7. The same as Fig. 6, but at $r_0=4$ fm and $\theta_0=60°$.

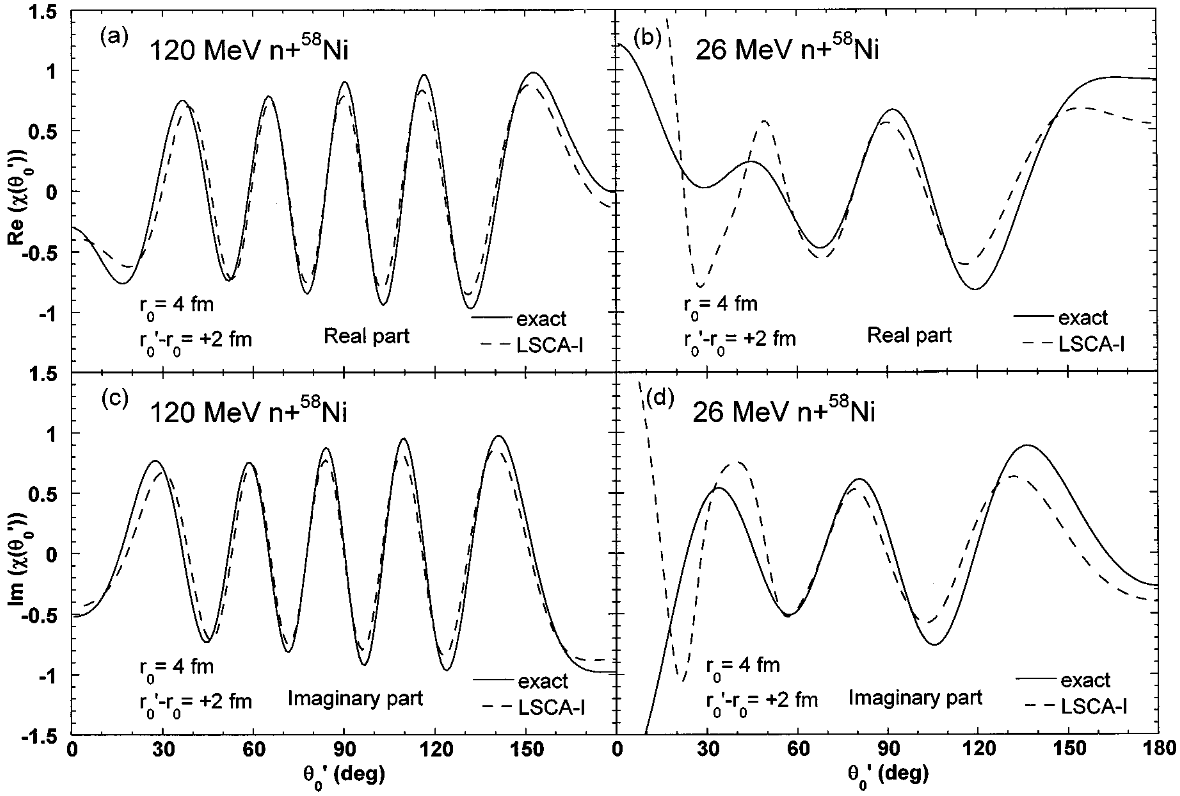

FIG. 8. The same as Fig. 6, but the distorted waves are plotted as a function of θ_0' at $r_0=4$ fm and $s=+2$ fm.

act'' distorted wave $\chi_c^{\text{exact}}(\mathbf{r}_0')$, a numerical solution of the Schrödinger equation for a distorting potential U_c, with the corresponding ''LSCA'' distorted wave $\chi_c^{\text{LSCA}}(\mathbf{r}_0')$ calculated from the RHS of Eq. (7), using the $\chi_c^{\text{exact}}(\mathbf{r}_0)$ under the condition that the directions of $\mathbf{r}_0'$ and $\mathbf{r}_0$ coincide. Two cases were considered: (a) variation of $s=|\mathbf{r}_0'-\mathbf{r}_0|$ at a fixed polar angle of $\mathbf{r}_0,\theta_0$ and (b) variation of θ_0 at a fixed values of s. For U_c, the global optical potential of Walter and Guss [14] was used for 26 MeV and that of Schwandt *et al.* [15] for 120 MeV.

The results for the case (a) at $r_0=2$ fm and 4 fm at $\theta_0=60°$ are shown in Figs. 6 and 7, respectively, and the results for the case (b) with $r_0=4$ fm and $s=+2$ fm are shown in Fig. 8. The real and the imaginary parts of the distorted waves are plotted in each figure, in the upper and lower panels, respectively. The solid lines represent the $\chi_c^{\text{exact}}(\mathbf{r}_0')$. The $\chi_c^{\text{LSCA}}(\mathbf{r}_0')$ calculated with only the real part of wave number for $\mathbf{k}_c$ on the RHS of Eq. (7) are shown by the long-dashed lines (LSCA-I) and those calculated with the complex wave numbers are shown by the short-dashed lines (LSCA-II). One can see from Figs. 6–8 that the LSCA is quite good at 120 MeV around the r_0 considered. In particular, it is noteworthy that the LSCA is still good at $r_0=4$ fm which is near the nuclear surface where the variation of U_c with $\mathbf{r}_0'$ is not so small. Also, LSCA-I and LSCA-II almost coincide over a wide range of $\mathbf{r}_0'$. This justifies the use of real local wave numbers in Eq. (7). These numerical tests show the validity of the LSCA at 120 MeV. The LSCA is worse at 26 MeV as expected. It should be noted, however, that it is still acceptable within a range $s\approx 1$ fm which is only slightly less than the ranges of the two-nucleon interaction and the nonlocal kernel $K(\mathbf{r},\mathbf{r}')$.

D. Quasielastic scattering in one-step process

All the one-step SCDW cross sections have peaks at angles that correspond to QES as already mentioned. In order to see the reason for this, we have examined where in the nucleus the first collision mainly takes place. The result is shown in Fig. 9 for ^{90}Zr(p,p') at 120 MeV. Each line corresponds to the one-step calculation with a given pair of lower and upper limits of radial integration in Eq. (13). The limits are varied in steps of 2 fm. It is seen that the contribution of the peripheral region of the nucleus corresponding to $r=4$–6 fm is predominant over a wide angular range, while the contribution of the nuclear interior tends to increase as the emission angle increases. The contribution of the region $r\geqslant 6$ fm provides the characteristic angular distribution with a peak at the QES angle. The reason for this is that the Fermi momentum is low there because the nucleon density is low. As a consequence, the incident proton interacts with target nucleons with small momenta. The peak seen in the one-step SCDW cross section is slightly shifted from the QES angle toward small angles. One reason for it is the contribution of the inner region where the Fermi motion of the target nucleons is not small. Another reason is the refraction of the projectile and ejectile by the distorting potentials. However, these effects are not large enough to compensate the sharp fall of the cross section at very small angles.

One of the reasons for the failure of the present SCDW calculations at very forward angles is that the most important contribution to the cross section there is due to collisions with large impact parameters, i.e., in the far out nuclear sur-

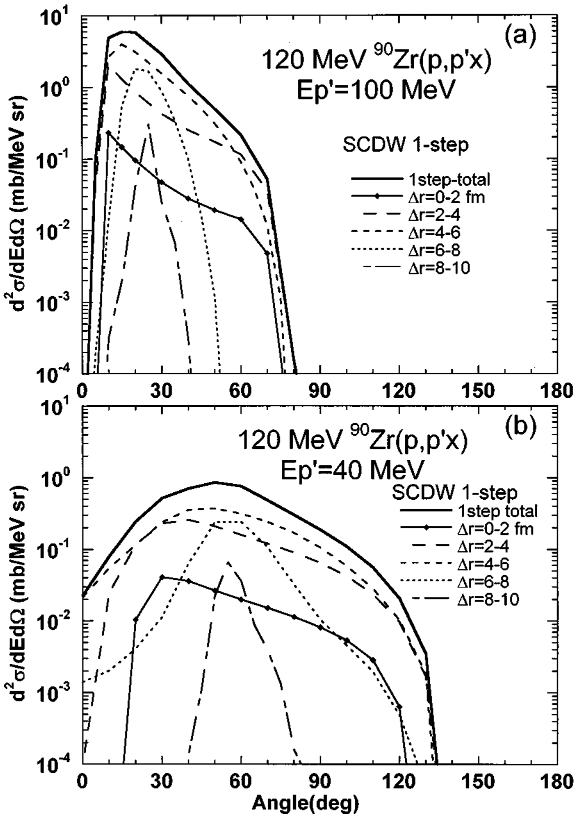

FIG. 9. Dependence of the SCDW one-step cross section on the location of N-N scattering in the nucleus. The reaction is ^{58}Ni($p,p'x$) at 120 MeV. The emission energies are (a) 100 MeV and (b) 40 MeV. Each curve corresponds to the one-step cross sections calculated with the lower and upper limits in the radial integration of Eq. (13) denoted in the figure. The thick lines are the total SCDW one-step cross sections.

face region where the nucleon density is very low. The LFG model is obviously inappropriate there. Nucleons in that region are mostly in the exponential tails of bound state wave functions as assumed, e.g., by Esbensen and Bertsch [29].

E. Effect of the nonlocality of distorting potentials

In the SCDW calculations, the nonlocality correction to distorted waves is made by means of the Perey factor [13]. Calculated cross sections without the nonlocality correction are shown in Fig. 10 for ^{58}Ni($p,p'x$) at 120 MeV. Overestimation of the magnitude of the cross sections is obvious, although the shape of angular distributions is not much different from those with the nonlocality correction. The effect increases as the proton emission energy decreases and the number of steps increases. The latter is because the number of the intermediate Green functions, each carrying two Perey factors, increases. For instance, three-step cross sections without the nonlocality correction are an order of magnitude larger than those with the correction in Fig. 10(b). Thus, the nonlocality correction in SCDW calculations is crucial to the agreement with experimental data in the absolute magnitude of cross sections, particularly at low emission energies.

The importance of the nonlocality correction was already mentioned by Negele and Yazaki [30] who showed that empirical values of the nucleon mean free path could be explained in terms of simple N-N scattering in the nuclear Fermi gas only if the effective mass is used for the nucleons. One of the reasons for use of the effective mass is the nonlocality of the nuclear mean field. In the present SCDW calculations, the leading particle and the target nucleons excited into the continuum move in phenomenological optical potentials which can be regarded as the equivalent local potentials of the "true," nonlocal optical potentials. Instead of the effective k mass of Ref. [30], we made the nonlocality correction by means of the Perey factor [13].

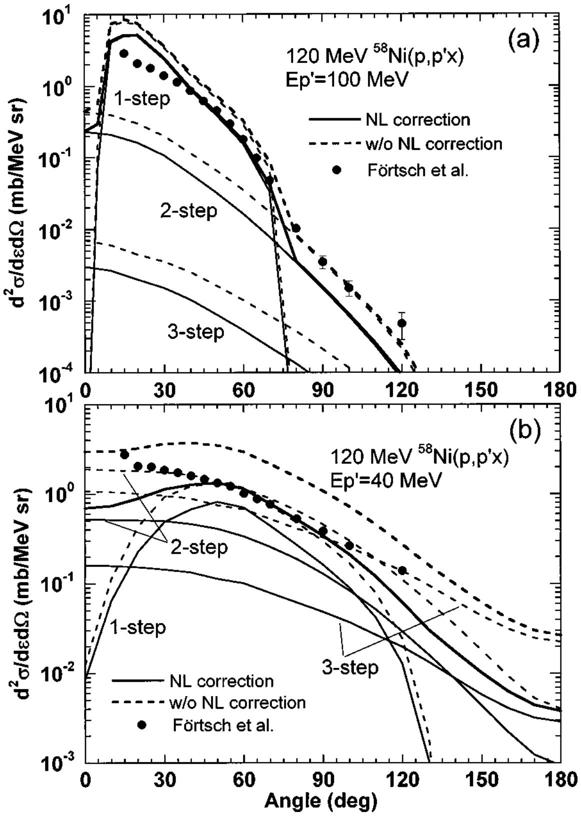

FIG. 10. Comparison of SCDW cross sections with (solid lines) and without (dashed lines) the nonlocality correction for the reaction ^{58}Ni($p,p'x$) at 120 MeV and two emission energies (a) 100 MeV and (b) 40 MeV. The thin lines represent individual stepwise contributions and the thick line represents their sum. The experimental data are taken from Ref. [27].

F. Sensitivity to the nucleon density distribution

We investigated the sensitivity of SCDW calculations to the nucleon density distribution. As an alternative to that used in Figs. 1–5, we calculated the proton and the neutron density distributions by means of the spherical Skyrme-Hartree-Fock (SHF) theory [31,32] with the Z_σ potential of Friedrich and Reinhard [31]. The densities of ^{90}Zr are shown in Fig. 11 together with the Woods-Saxon one used in Figs. 1–5. The two densities are almost identical in the peripheral region, from 4 to 6 fm, some differences appearing in the nuclear interior.

In Fig. 12, the calculated double differential cross sections of one-step process in ^{90}Zr($p,p'x$) at 160 MeV are shown for the Wood-Saxson density distribution with Negele's parameters (dashed lines) and the SHF density distribution

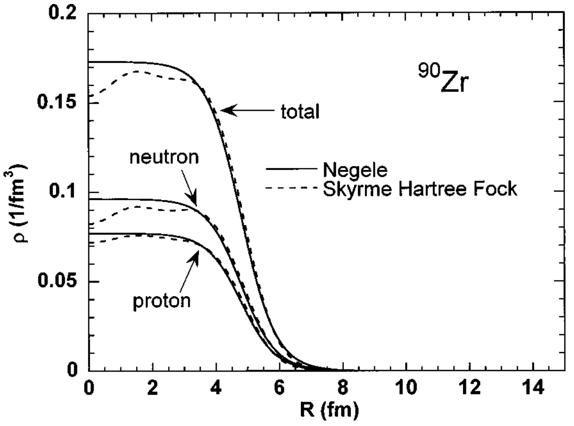

FIG. 11. The calculated nucleon density distributions of ^{90}Zr. The solid and dashed lines represent the density distribution of the Woods-Saxon shape with Negele's geometrical parameters and that calculated with the Skyrme-Hartree-Fock (SHF) theory, respectively.

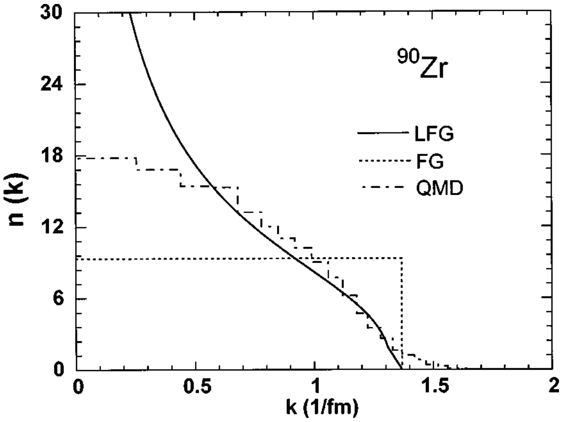

FIG. 13. The momentum distribution of target nucleons. The solid and dotted curves represent the momentum distributions based on the local Fermi gas (LFG) model and the infinite Fermi gas (FG) model. The result of QMD plotted by the dash-dotted histogram is taken from Ref. [6].

(solid lines). In these calculations, separate Fermi momenta $k_F^p(\mathbf{r})$ and $k_F^n(\mathbf{r})$ were used for protons and neutrons, instead of the average Fermi momentum. We confirmed, however, that the difference between the calculations with the separate and the average Fermi momenta is negligible. Figure 12 shows that there is no appreciable difference between the two calculations with the two density distributions. This is easily understood because the dominant contribution comes from the surface region of the nucleus as shown in Fig. 9 where the two density distributions are almost identical as shown in Fig. 11. Also, for two- and three-step processes, the difference in the nucleon density distribution causes negligible effect on the corresponding cross sections. Thus, the sensitivity of SCDW calculations to the nucleon distributions is very weak.

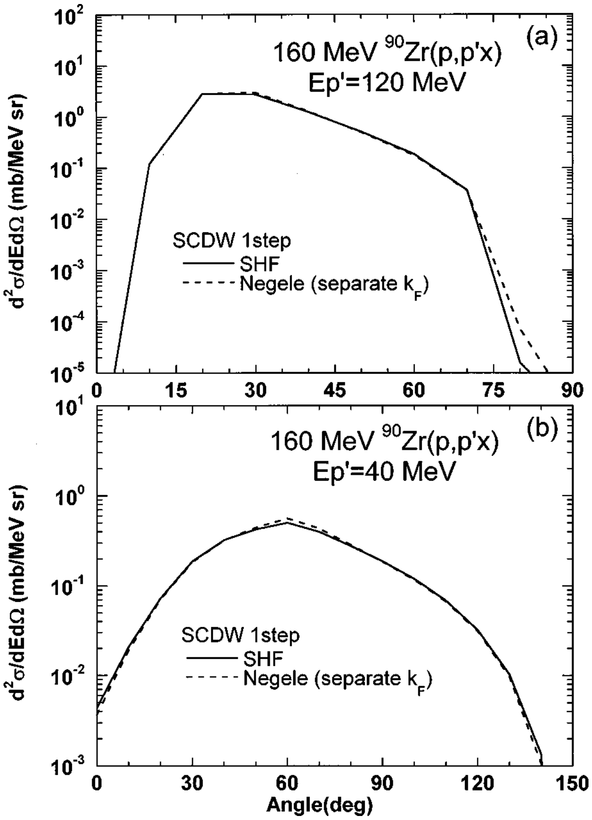

FIG. 12. Comparisons of SCDW one-step cross sections of the reaction ^{90}Zr$(p,p'x)$ at 160 MeV calculated with two different nucleon density distributions: the Woods-Saxon one with Negele's parameters (dashed lines) and the Skyrme-Hartree-Fock one (solid lines).

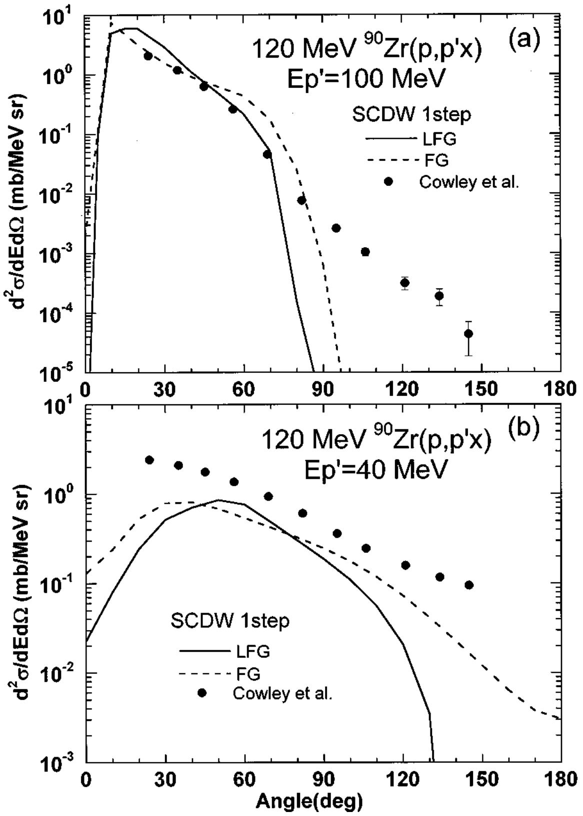

FIG. 14. Comparisons of SCDW one-step cross sections of the reaction ^{90}Zr$(p,p'x)$ at 120 MeV calculated with two different momentum distributions: the LFG one (solid lines) and the FG one (dashed lines). The experimental data are taken from Ref. [24].

G. Sensitivity to the nucleon momentum distribution

As shown in Sec.III B, the SCDW model fails to reproduce cross sections at very small and large angles. Since the differential cross section at a fixed emission energy is a function of momentum transfer, the angular distribution must depend on the momentum distribution of the target nucleons. We investigated the dependence by calculating one-step cross sections under different assumptions of the momentum distribution. Figure 13 shows the nucleon momentum distribution of ^{90}Zr in three different models: the infinite Fermi gas (FG) model, the local density Fermi gas (LFG) model, and quantum molecular dynamics (QMD) [6]. The FG model gives a uniform distribution up to the Fermi momentum k_F. The LFG momentum distribution has a large fraction of nucleons with small k, and becomes infinite at $k=0$. The differences between QMD and the LFG model appears at momenta less than 0.5 fm^{-1} and at momenta larger than $k_F=1.37$ fm^{-1}, the Fermi momentum for the normal nuclear density.

In Fig. 14, the one-step SCDW cross sections for ^{90}Zr(p,p') at 120 MeV calculated with the LFG and FG models are compared. The solid and dashed curves represent the SCDW calculations with the LFG and FG models, respectively. Figures 13 and 14 show that the nucleon momentum distribution strongly affects the shape of the one-step angular distribution. The increase in high-momentum components in the nuclear momentum distribution leads to an enhancement of the cross sections at large angles, and decrease in low-momentum components results in a shift of the QES peak toward smaller angles. This suggests that use of realistic single particle wave functions in a finite potential rather than the LFG model will improve the SCDW cross sections at large and small angles.

H. Use of in-medium *N*-*N* cross sections

We recently calculated *N*-*N* cross sections in the nuclear medium by means of the non-relativistic Brueckner *G* matrix based on the Paris potential, and parametrized them as a function of incident energy and nucleon density [20]. The in-medium *N*-*N* cross sections calculated with the parameter set given in Table II of Ref. [20] were used for the *N*-*N* cross section. Figure 15 shows the result of the calculations for ^{58}Ni$(p,p'x)$ reactions at 120 and 65 MeV together with the ones obtained with the free *N*-*N* cross sections. No appreciable difference is found between the two calculations, even at 65 MeV at which the in-medium cross sections at the normal nuclear density ρ_0 are much reduced from the free ones. This is because the one-step process occurs mainly in the surface region of the nucleus where the density is low, as discussed in Sec. III D, so that the in-medium cross sections are not much different from the free ones.

I. Comparison with other model

In this subsection, we compare the SCDW calculations with the results of the other models already mentioned, AMD [7], QMD [6], FKK [6,23,34,35], and TUL [4], and discuss similarities and differences.

First, a comparison with AMD [7] is made for ^{58}Ni$(p,p'x)$ at 120 MeV in Fig. 16. Agreement is generally good, although the SCDW three-step cross sections are somewhat smaller than the AMD ones. It is noticeable that the AMD one-step cross sections also show peaks near the QES angles, though slightly shifted forward. Such peaks do not appear in the cross sections in QMD.

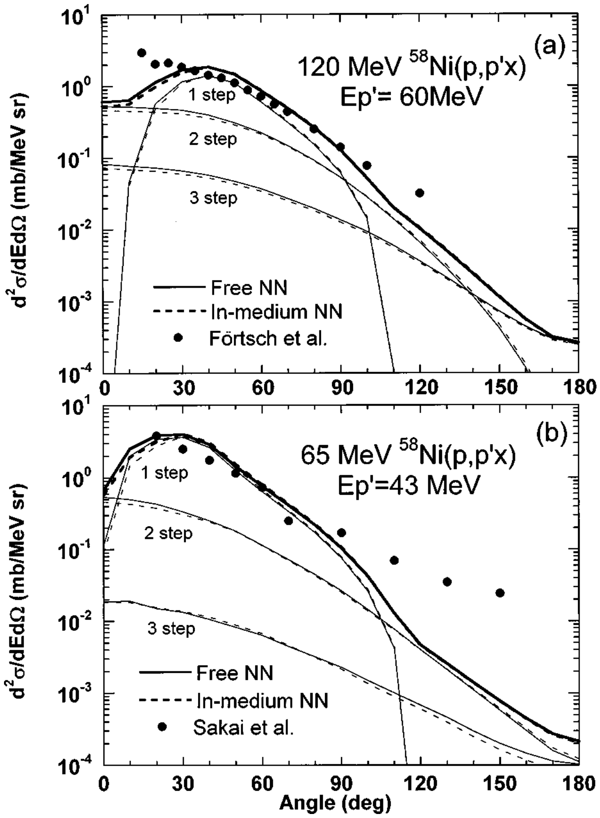

FIG. 15. Comparisons of SCDW cross sections calculated with in-medium *N*-*N* cross sections of Ref. [20] (solid lines) and those with the free *N*-*N* cross sections (dashed lines) for the reaction ^{58}Ni$(p,p'x)$ at (a) 120 MeV and (b) 65 MeV. The experimental data are taken from Refs. [27] and [33].

Second, the SCDW model and QMD are compared in Figs. 16 and 17. One sees some differences in one-step angular distributions, in particular at backward and very forward angles. The QMD one-step cross sections show forward peaks without the steep fall near 0° that is seen in the SCDW ones. It was maintained in Ref. [6] that the behavior of QMD one-step cross sections near 0° was strongly affected by the refraction of the incident and outgoing particles by the mean field. However, the SCDW calculations also took account of the refraction by the distorting potentials, and the effect was small. The difference at backward angles is due mainly to the difference in the momentum distribution of target nucleons as already mentioned. As shown in Fig. 13, QMD, unlike the LFG model, includes target nucleons with momenta higher than the Fermi momentum. As for the two- and the three-step cross sections, the SCDW and QMD cross sections are similar in shape, although the SCDW model yields smaller cross sections at the highest emission energy than QMD.

Third, a comparison of the SCDW model with the FKK model [6] is made in Fig. 17. A considerable difference in one-step cross sections is seen between the predictions of the

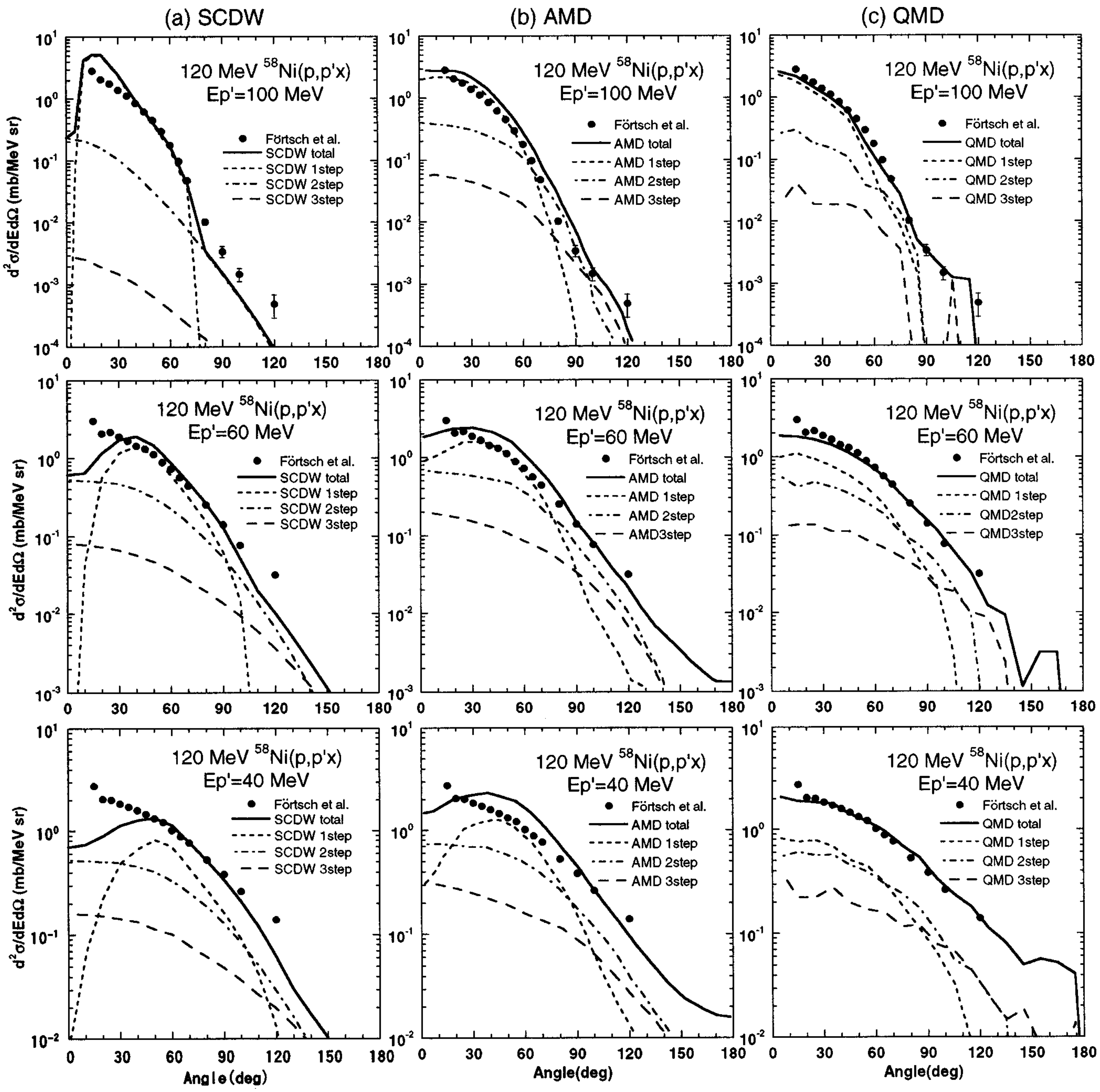

FIG. 16. Comparisons of SCDW calculations with AMD and QMD calculations for the reaction ^{58}Ni$(p,p'x)$ at 120 MeV. The AMD and QMD results are taken from Refs. [7,6] and include multistep components higher than three-step in total cross sections given by the solid curves. The experimental data are taken from Ref. [27].

two models, although the higher-step cross sections do not differ as much. The FKK model gives steeper fall of one-step cross sections towards large angles than the SCDW model. The relative contributions of the two- and the three-step processes at backward angles are larger in the FKK model than in the SCDW model. The results shown in Fig. 16 can also be compared with the FKK analysis of ^{58}Ni$(p,p'x)$ by Richter *et al.* [34]. They showed that at high emission energies, such as 100 MeV, the cross sections in the angular region from 40° to 70° could not be reproduced by the FKK model alone. The discrepancy could be removed by the addition of a QES knockout contribution calculated with the DWIA. Our SCDW prediction is in quite good agreement with the experimental data at the corresponding angular region. The QES component is automatically taken into account because experimental *N-N* cross sections which include exchange process in the *N-N* scattering are used. For the case of lower incident energies, one can compare the result for ^{90}Zr$(p,p'x)$ at 80 MeV in Fig. 3 with the recent FKK analysis of Ref. [35]. The FKK calculation shows a slight overprediction of cross sections at backward angles, while the SCDW considerably underestimates them in the same angular region as already discussed.

Finally, a comparison of the SCDW model with the TUL model [4] is shown for the ^{209}Bi$(p,p'x)$ reaction at 62 MeV in Fig. 18. The results of the SCDW and TUL models are

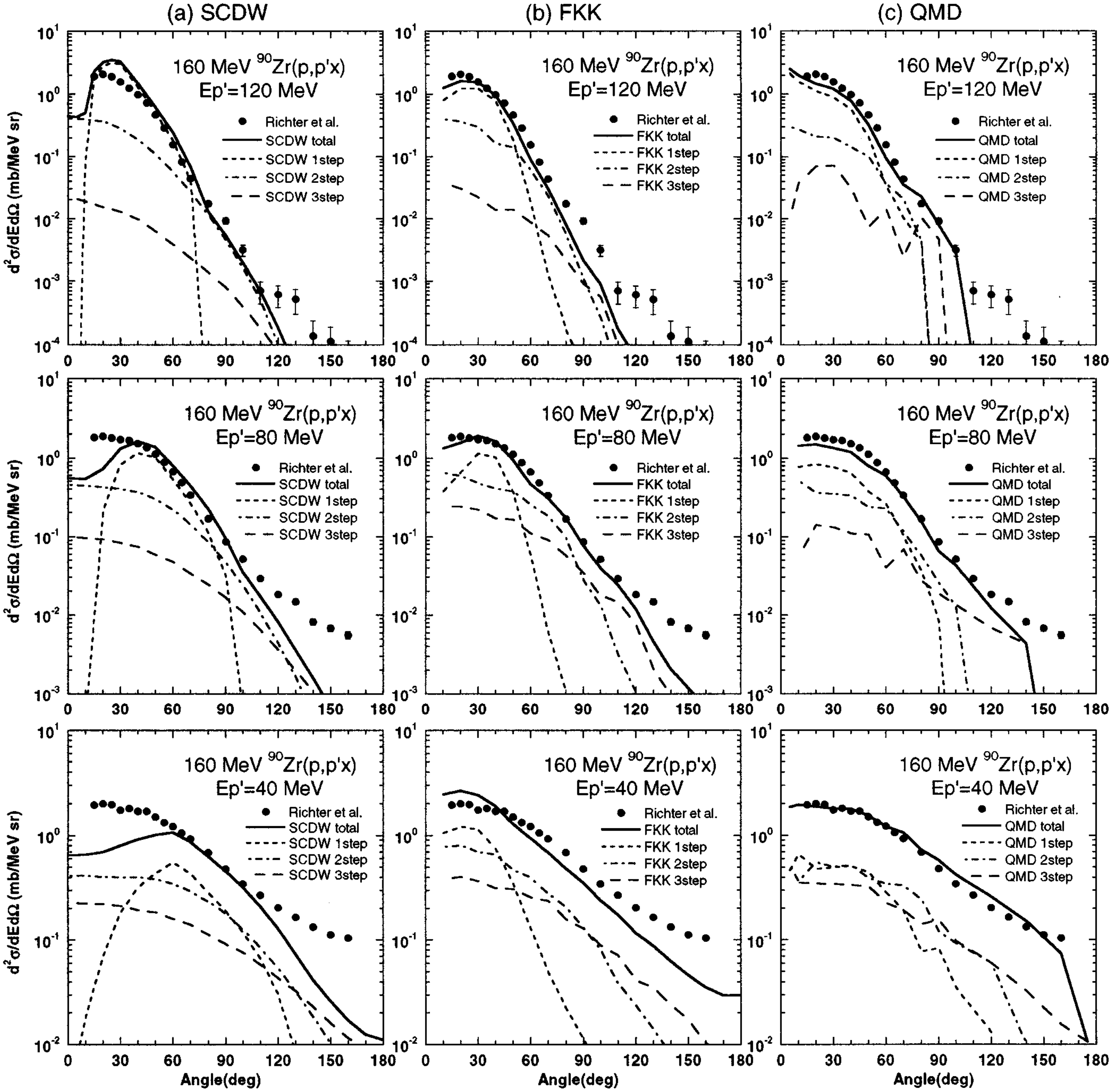

FIG. 17. Comparisons of SCDW calculations with FKK and QMD calculations for the reaction ^{90}Zr($p,p'x$) at 160 MeV. The FKK and QMD results are taken from Ref. [6]. The total FKK cross sections include multistep components up to five steps. The experimental data are taken from Ref. [23].

given by the thick and thin curves, respectively. Note that the calculation by the TUL model is restricted to one- and two-step processes. The results of the SCDW and TUL models are same in the intermediate angular region from 30° to 90°, although there are distinct differences at very small and large angles. This figure also shows that the one-step process is predominant in this reaction.

From the comparisons of the SCDW model with the other four MSD models, we conclude that the calculated angular distribution of the one-step process is strongly model dependent, but those of the multistep processes are not. In addition, the relative magnitudes of the contributions of individual multisteps are rather similar in all the models compared.

IV. SUMMARY AND CONCLUSIONS

The SCDW model was extended to include three-step processes in multistep direct inelastic scattering, and to deal with charge exchange reactions.

Calculations of the cross sections of MSD processes in ($p,p'x$) and (p,nx) on ^{90}Zr at 80, 120, and 160 MeV, ^{58}Ni($p,p'x$) at 65 and 120 MeV, and ^{209}Bi($p,p'x$) at 62 MeV were calculated by means of the extended SCDW model and the results were compared with the experimental data. The result shows that the cross sections calculated with no free adjustable parameter are in overall good agreement with the data, although underpredicted at very small and

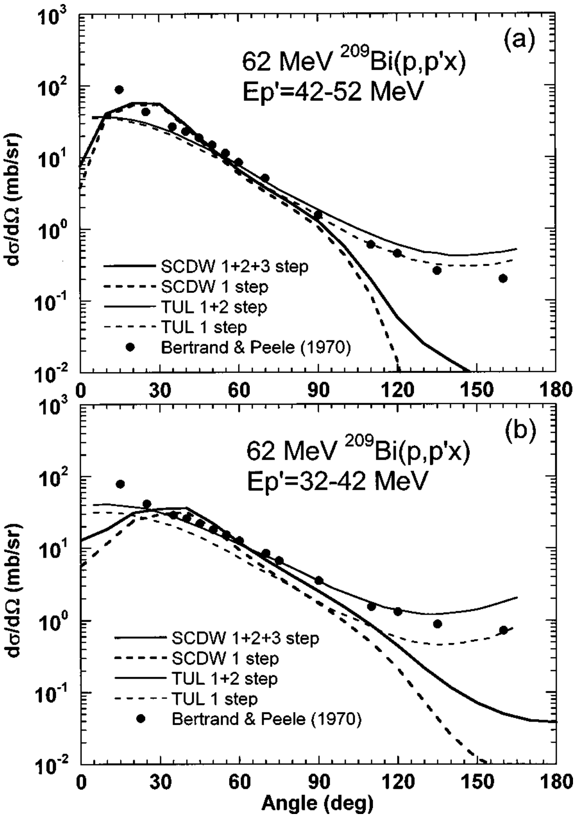

FIG. 18. Comparisons of SCDW calculations (thick curves) with TUL calculations (thin curves) for the reaction ^{209}Bi$(p,p'x)$ at 62 MeV. The TUL result is taken from Ref. [4]. The experimental data are taken from Ref. [28].

large angles. The contribution of the two-step process dominates the calculated cross sections at very forward and backward angles and that of the three-step process at even larger angles. They much improve the agreement with the experimental data at those angles, but are not large enough to entirely compensate the disagreement of one-step cross sections. It is found that much of the one-step process is due to N-N collisions in the surface region of the nucleus. Cross sections at very small and large angles are also found to depend strongly on the momentum distribution of target nucleons. The failure of the model at those angles is at least partly due to the failure of the LFG model in the nuclear surface region in which the nucleon density is relatively low. In addition, contributions of four-step and higher-step processes might be partly responsible for the underprediction at backward angles. The nonlocality correction to the distorting potentials is essential for the reasonable agreement with the data in the absolute magnitude of cross sections, in particular at low emission energies. In contrast, use of in-medium N-N cross sections little changes either the shape of angular distribution or the magnitude of cross sections from those calculated with the free N-N cross sections.

The comparison of the SCDW calculations with the AMD, QMD, FKK, and TUL calculations shows that the shapes of one-step angular distributions are different among the models, but the multistep components are rather similar in angular distributions and in the relative magnitude of the cross sections of individual steps.

In conclusion, the results reported in the present paper are encouraging enough for further improvements of the SCDW model, such as the use of more realistic single particle wave functions, extension of the domain of applications to a wider range of incident energies and target mass numbers, and inclusion of nuclear spins.

ACKNOWLEDGMENTS

We wish to thank Dr. S. Chiba, Dr. Tomoyuki Maruyama, Dr. Toshiki Maruyama, Dr. K. Niita, and Dr. A. Iwamoto in JAERI, and Prof. H. Horiuchi and the late Dr. E.I. Tanaka in Kyoto University for their correspondences about QMD and AMD calculations and many stimulating discussions. We also wish to thank Dr. M.B. Chadwick for his valuable discussion on FKK calculations. We are much indebted to Prof. Y. Akaishi and Prof. Y.R. Shimizu for their kind help and advice on Monte Carlo calculations. We also acknowledge the financial aid of RCNP, Osaka University, for the computation and the use of parallel computers at JAERI. This work was supported in part by a Grant-in-Aid for Scientific Research of the Ministry of Education, Science, and Culture (Nos. 07640416 and 09558059).

---

[1] See, for example, E. Gadioli and P. E. Hodgson, *Pre-Equilibrium Nuclear Reactions* (Oxford University Press, New York, 1992).
[2] M. L. Goldberger, Phys. Rev. **74**, 1269 (1948).
[3] H. Feshbach, A. Kerman, and S. Koonin, Ann. Phys. (N.Y.) **125**, 429 (1980).
[4] T. Tamura, T. Udagawa, and H. Lenske, Phys. Rev. C **26**, 379 (1982).
[5] H. Nishioka, H. A. Weidenmüller, and S. Yoshida, Ann. Phys. (N.Y.) **183**, 166 (1988).
[6] S. Chiba, M. B. Chadwick, K. Niita, T. Maruyama, T. Maruyama, and A. Iwamoto, Phys. Rev. C **53**, 1824 (1996).
[7] E. I. Tanaka, A. Ono, H. Horiuchi, T. Maruyama, and A. Engel, Phys. Rev. C **52**, 316 (1995).
[8] A. J. Koning and J. M. Akkermans, Ann. Phys. (N.Y.) **208**, 216 (1991).
[9] Y. L. Luo and M. Kawai, Phys. Lett. B **235**, 211 (1990); Phys. Rev. C **43**, 2367 (1991).
[10] M. Kawai and H. A. Weidenmüller, Phys. Rev. C **45**, 1856 (1992).
[11] Y. Watanabe and M. Kawai, Nucl. Phys. **A560**, 43 (1993).
[12] J. J. Griffin, Phys. Rev. Lett. **17**, 478 (1966).
[13] F. G. Perey and B. Buck, Nucl. Phys. **32**, 353 (1962).
[14] R. L. Walter and P. P. Guss, in *Proceedings of the International Conference on Nuclear Data for Basis and Applied Science,* Santa Fe, New Mexico, 1985, edited by P. G. Young (Gordon and Breach, New York, 1986), p. 1075.
[15] P. Schwandt, H. O. Meyer, W. W. Jacobs, A. D. Bacher, S. E. Vigdor, and M. D. Kaitchuck, Phys. Rev. C **26**, 55 (1982).
[16] D. G Madland, in *Proceedings of a Specialists' Meeting on Preequilibrium Reactions,* Semmering, Austria, 1988, edited

by B. Strohmaier (OECD, Paris, 1988), p. 103.
[17] J. W. Negele, Phys. Rev. C **1**, 1260 (1970).
[18] K. Kikuchi and M. Kawai, *Nuclear Matter and Nuclear Reactions* (North-Holland, Amsterdam, 1968), p. 33.
[19] H. W. Bertini, Oak Ridge National Laboratory Report No. ORNL-3383, 1963.
[20] M. Kohno, M. Higashi, Y. Watanabe, and M. Kawai, Phys. Rev. C **57**, 3495 (1998).
[21] C. B. Haselgrove, Math. Comput. **15**, 323 (1961).
[22] Y. Akaishi (private communication).
[23] W. A. Richter, A. A. Cowley, G. C. Hillhouse, J. A. Stander, J. W. Koen, S. W. Steyn, R. Lindsay, R. E. Julies, J. J. Lawrie, J. V. Pilcher, and P. E. Hodgson, Phys. Rev. C **49**, 1001 (1994).
[24] A. A. Cowley, A. van Kent, J. J. Lawrie, S. V. Förtsch, D. M. Whittal, J. V. Pichler, F. D. Smit, W. A. Richter, R. Lindsay, I. J. van Heerden, R. Bonetti, and P. E. Hodgson, Phys. Rev. C **43**, 678 (1991).
[25] M. Trabandt, W. Scobel, M. Blann, B. A. Pohl, R. C. Byrd, C. C. Foster, and R. Bonetti, Phys. Rev. C **39**, 452 (1989).
[26] W. Scobel, M. Trabandt, M. Blann, B. A. Pohl, B. R. Remington, R. C. Byrd, C. C. Foster, R. Bonetti, C. Chiesa, and S. M. Grimes, Phys. Rev. C **41**, 2010 (1990).
[27] S. V. Förtsch, A. A. Cowley, J. J. Lawrie, D. M. Whittal, J. V. Pilcher, and F. D. Smit, Phys. Rev. C **43**, 691 (1991).
[28] F. E. Bertrand and R. W. Peele, Phys. Rev. C **8**, 1045 (1973).
[29] H. Esbensen and G. F. Bertsch, Ann. Phys. (N.Y.) **157**, 255 (1984).
[30] J. W. Negele and K. Yazaki, Phys. Rev. Lett. **47**, 71 (1981).
[31] J. Friedrich and P.-G. Reinhard, Phys. Rev. C **33**, 335 (1986).
[32] P.-G.Reinhard, *The Skyrme-Hartree-Fock Model of the Nuclear Ground State*, *Computational Nuclear Physics 1* (Springer-Verlag, Berlin, 1991), Chap. 2, p. 28.
[33] H. Sakai, K. Hosono, N. Matsuoka, S. Nagamachi, K. Okada, K. Maeda, and H. Shimizu, Nucl. Phys. **A344**, 41 (1980).
[34] W. A. Richter, A. A. Cowley, R. Lindsay, J. J. Lawrie, S. V. Förtsch, J. V. Pilcher, R. Bonetti, and P. E. Hodgson, Phys. Rev. C **46**, 1030 (1992).
[35] A. J. Koning and M. B. Chadwick, Phys. Rev. C **56**, 970 (1997).